PNAS
www.pnas.org

Supplementary Information for

Evidence of magnetism-induced topological protection in the axion insulator candidate $EuSn_2P_2$

Gian Marco Pierantozzi, Alessandro De Vita, Chiara Bigi, Xin Gui, Hung-Ju Tien, Debashis Mondal, Federico Mazzola, Jun Fujii, Ivana Vobornik, Giovanni Vinai, Alessandro Sala, Cristina Africh, Tien-Lin Lee, Giorgio Rossi, Tay-Rong Chang, Weiwei Xie, Robert J. Cava, and Giancarlo Panaccione

Corresponding author: Robert J. Cava
Email: rcava@princeton.edu

This PDF file includes:

Supplementary Information Text

Scanning Tunneling Microscopy investigation. After UHV cleavage, the sample topography was investigated by STM at 77 K. Fig. S1a presents a typical image of the surface, where single surface steps separate large terraces of hundreds of nm in size. The atomic step height, evaluated on the basis of 18 intensity line profiles from 6 large-scale images, was found to be 8.8±0.3 Å. Such height corresponds to the distance between homonuclear planes in the ABC stacking along the rhombohedral *c* axis of the crystal lattice (8.7 Å) (1). No other step height was found in random sites of the crystal, indicating that the atomic termination is homogeneous on the entire cleaved surface. Fig. S1b shows an atomically resolved image of one flat terrace. The surface is composed by atoms arranged in a triangular 2D lattice, with occasional defects (dark features in the image) ascribable to single-atom vacations. From intensity line profile and Fast Fourier Transform analysis of STM high-resolution images, an on-plane interatomic distance of 4.0±0.1 Å can be extrapolated, confirming a triangular 2D lattice geometry compatible with the atomic arrangement of the homonuclear planes, as can be seen by the top view of the crystal structure (Fig. S1c). All planes have the same geometry, so STM cannot clarify what kind of atomic termination is probed. Nonetheless, atomically resolved large-scale images showed no change or lateral shift in the atomic texture of the surface along tens of nm, thus confirming the homogeneity of the surface atomic plane.

Scanning Tunneling Spectroscopy investigation. In Fig. S2 the normalized dI/dV characteristic of the $EuSn_2P_2$ surface is presented. The spectrum presents three distinct main contributions: one occupied band below -0.8 V (in orange), a partially occupied band with roughly constant density of states that stretches from -0.8 V to +0.3 V (in green), an empty band with high density of states that rises above +0.6 eV (in blue). These three features can be identified by comparing the data with the theoretical calculations and the ARPES data presented in Fig. 1 in main text: the first one is the Eu *4f* band, the second one is the P *p* band (both bulk and surface states), the third one is the Sn *p* band. The dI/dV characteristics collected on several points of the sample with different tip conditioning showed no significant variations.

Spin resolved ARPES: Eu localized ferromagnetism. In Fig. S4 spin-resolved ARPES is employed to investigate the spin polarization of Eu *4f* states at 15 K along all three vectorial directions, completing the result reported in Fig.2c in main text. The polarization around 20% in the *x* direction (Fig. S4a), is accompanied by the absence of a detectable polarization along *y* (Fig. S4b) and in the out-of-plane direction (Fig. S4c). This result justifies the picture in the inset of Fig. 2c, showing the magnetic moments aligned along the *x* direction. It is worth to stress again that, since $EuSn_2P_2$ presents an A-type antiferromagnetism, the Eu magnetic momenta in the adjacent layer below are oppositely aligned with respect to the outer one, so that the spin polarization measured by ARPES is just a lower limit for the spin polarization within a single Eu layer.

ARPES: photon energy and temperature dependence. The matrix-element of the various bands highlighted in Fig. 1 in main text presents different dependences on the photon energy, allowing to enhance a band with respect to another by performing the measurement at a certain energy. As can be seen in the constant-energy cuts at Fermi level and slightly below, measured at photon energies in the range 27-50 eV (Fig. S5), the P-derived states σ and P are better distinguished at 27 eV, whereas their intensity decrease at higher photon energy, almost disappearing above 30 eV, thus justifying the choice of 27 eV for the spin polarization measurement. No relevant changes of the band structure and, in particular, no modification of the P state, are observed upon the magnetic transition, as can be seen by the ARPES maps along $\bar{\Gamma} - \bar{K}$ and $\bar{\Gamma} - \bar{M}$ directions at 15 and 80 K (i.e., respectively below and above $T_{Néel}$) in Fig. S6.

Robustness of surface-state spin texture. The spin texture of the surface state P, as well as the surface resonance σ, is maintained also above $T_{Néel}$, i.e. at 80 K, as displayed in Fig. S7a-b: the result is identical to the one found at 15 K (see Fig. 3f-g in main text), i.e. a sign inversion of the *y* component of the spin of both bands when measuring at opposite momentum. This proves

that the spin polarization of the surface state is independent on the magnetic order. In Fig. S7c-d we show the same spin polarization measurement on another spot of the sample surface, where the surface resonance σ' has negligible intensity. The surface state P presents anyway the same spin texture, with around 10% of spin polarization for the *y* component and sign reversal at opposite momentum, demonstrating the robustness against surface inhomogeneity. Both P and σ bands are typical features of the P termination, as discussed in main text (see Fig. 1i in main text). The reason for the variation of their intensity ratio across the surface (shown in the constant energy cuts in Fig. S8) could be ascribed to a surface inhomogeneity, which could limit the coherence of the surface-derived states. These spectra also show that the P band is well visible after some days in UHV, with only a slight variation of k_F due to different level of hole-doping.

Direction of the spin of surface state. The spin polarization measurements of the surface states presented both in Fig. 3f-g in main text and in Fig. S7 regard only the *y* component of the spin vector (i.e. parallel to k_y direction according to the reference frame used through all the paper). In Fig. S9 we show all the three components, measured at a fixed momentum value, highlighted as a magenta spot in the Fermi surface map in the inset: the *y* component (Fig. S9a) has the value of 10% both on P and σ bands, in agreement with the results in Fig. S7, whereas negligible polarization is observed in the orthogonal in-plane *x* direction for both P and σ band (Fig. S9b). This result allows to justify the picture in Fig. 3e in main text for what concerns the in-plane projection of the spin of the P state. A negligible out-of-plane component is observed for the P band, whereas the surface resonance σ has a tiny projection along this direction (Fig. S9c).

Topological protection of the surface state. Bulk-boundary correspondence is one of recognized concept of the topological band theory, which refers to the notion that the boundary between two insulating states with different topological indices (for instance nontrivial topological state and the vacuum) must display metallic topological surface or edge states at the boundary. Therefore, (*d*-1)-dimensional gapless states appear in the boundary of *d*-dimensional system (2, 3). This concept has been extended to higher-order topological system, in which gapless topological states arise at (*d*-2)-dimensional boundary in a *d*-dimensional system, such as higher-order TI and axion insulator (4, 5). Based on this concept, we may expect that $EuSn_2P_2$ displays the gapped surface states on all crystal faces and shows the gapless chiral hinge states between two gapped surfaces, because $EuSn_2P_2$ present nontrivial axion coupling according to the calculation of Z_4 invariant, $Z_4 = 2$. As expected, our calculation shows a gapped surface state on (001) along $\bar{\Gamma} - \bar{K}$ direction (Fig. S10b). However, the topological boundary states are not only protected by Z_4 invariant in $EuSn_2P_2$, but also Z_2 and MCN n_M. Therefore, nontrivial Z_2 number guarantees the existence of a gapless Dirac surface states on the side surface of $EuSn_2P_2$, i.e. (010). This is confirmed by our calculation in Fig. S10c. In addition, Mirror Chern number $n_M = 1$ on $k_x = 0$ mirror plane protects a gapless surface state on (001) surface along $\bar{\Gamma} - \bar{M}$ direction, as confirmed by our calculation in Fig. S10d. In contrast to Dirac cone on the side surface, the Dirac point on (001) plane is not pinned on the $\bar{\Gamma}$ point, but lies in the in-plane direction projection of the mirror plane, i.e. along k_y. This is because the time-reversal symmetry breaking creates a gap in the Dirac state at time-reversal invariant momenta, but the additional reflection symmetry allows the gapless band crossing on a point of the mirror plane.
Therefore, all the crystal faces in $EuSn_2P_2$ under in-plane AFM magnetic order are gapless, despite the origin of the gapless state on the side surface and the top surface are protected by different topological invariants.

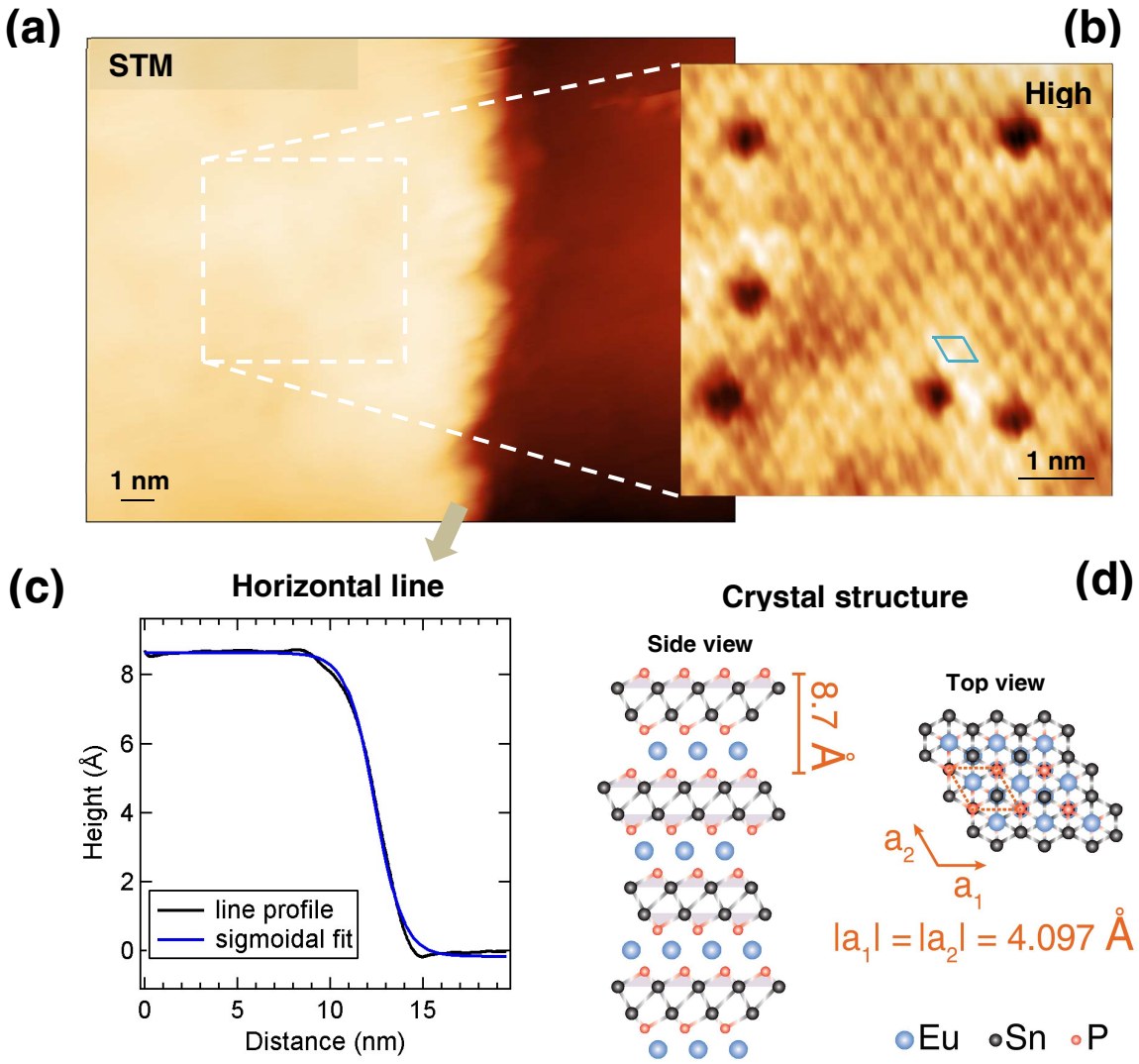

Fig. S1. STM. (a) Topographic STM image of two terraces separated by a surface step. The high-resolution inlay in (b) shows the atomic arrangement of the surface. The trigonal lattice unit cell is highlighted in blue. Image parameters: (a) bias -0.9 V, current 4.0 nA; (b) bias +0.2 V, current 6.0 nA. (c) Intensity line profile across the step and fit with a sigmoidal curve of height 8.8 Å. (d) Side and top view of the crystal structure. The height of the homonuclear planes and the dimension of the surface trigonal lattice unit cell are shown.

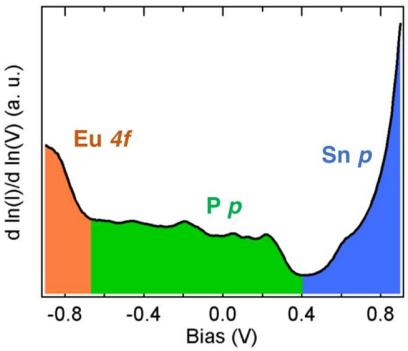

Fig. S2. Normalized dI/dV characteristic of EuSn2P2 surface. The dI/dV characteristics, normalized respect to the relative I/V curve, offers a direct measurement of the electronic density of states. The spectrum presents three main features, highlighted with different colors, that can be associated to the bands indicated in the taglines. T = 77 K.

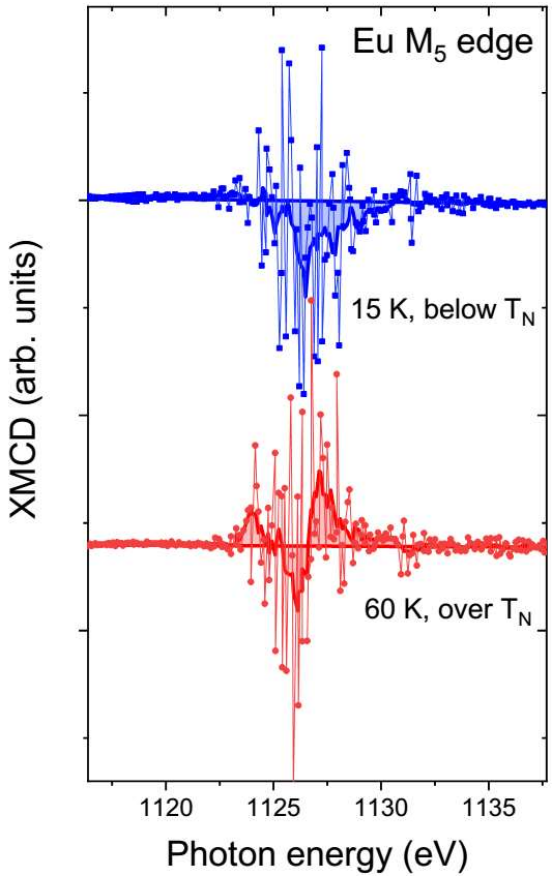

Fig. S3. X-ray Magnetic Circular Dichroism (XMCD) below and above T_N. Normalized XMCD obtained as the difference between absorption spectra with circular right and circular left polarizations, at the M_5 edge. The graphs shown on top (blue curve) and bottom (red curve) are respectively measured at T = 15 K and 60 K, i.e. below and above $T_{Néel}$. The dichroic signal at 15 K has an area coverage mostly below zero, whereas at 60 K the signal is equally distributed above and below zero, proving that, within our experimental resolution, the magnetic order vanishes as expected above $T_{Néel}$. Points with thin lines represent raw data, thick solid lines are obtained after a smoothing procedure.

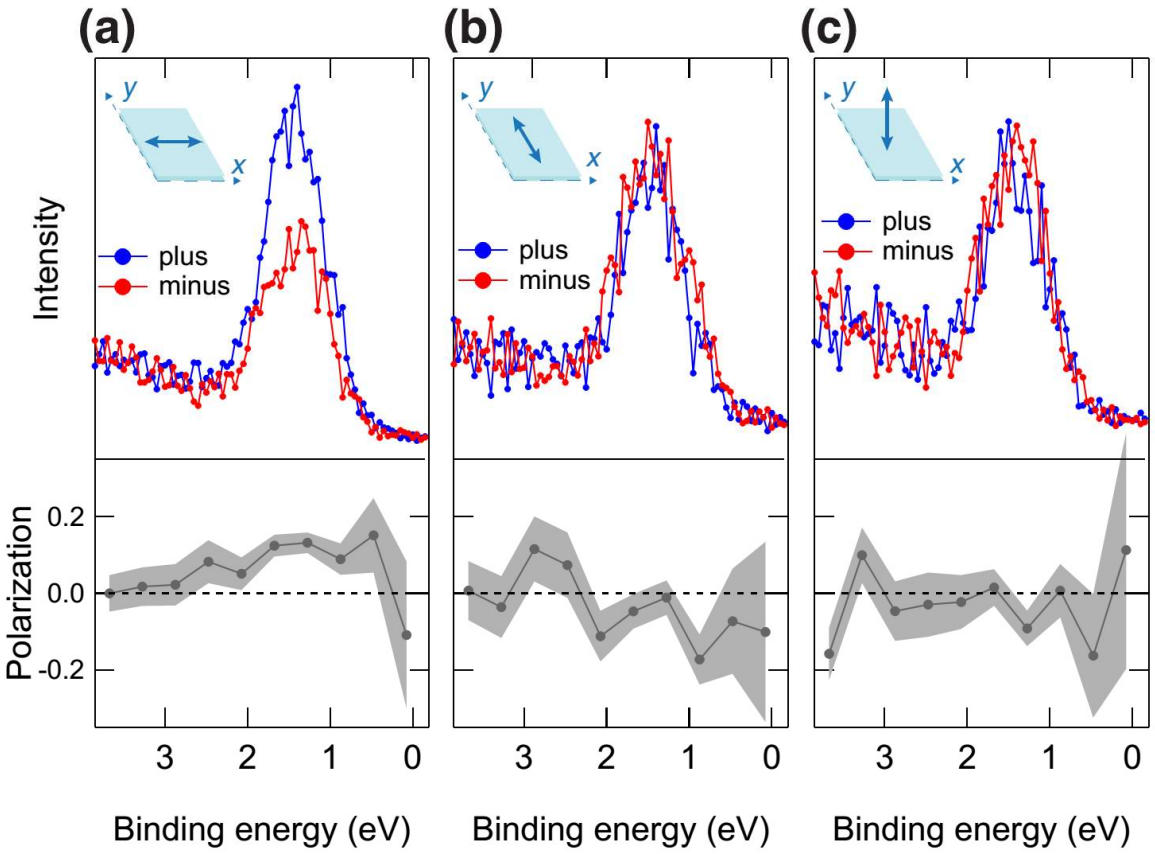

Fig. S4. Spin-resolved EDCs of Eu 4f. Spin-resolved photoemission spectra and spin polarization of a $EuSn_2P_2$ sample acquired at 15 K. Blue and red curves stand for the two opposite spin directions; the gray curves plot the spin polarization. The inset in each panel shows the direction with respect to the sample surface along which the spin was probed for each spin-resolved measurement: (a-b) in-plane (*x*, *y* directions), respectively in panel (a) and (b), (c) out-of-plane (*z* direction) in panel (c). All spectra were measured at the position in k-space marked in Fig. 3c in the main text.

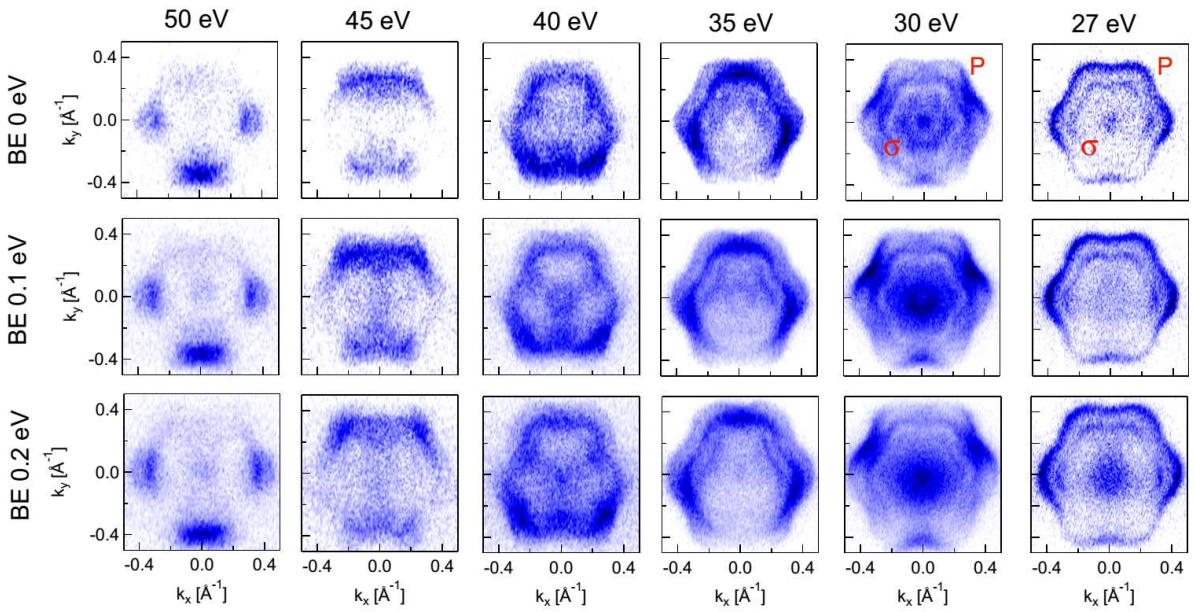

Fig. S5. Photon-energy dependent ARPES. ARPES isoenergetic cuts at different binding energies (BE) (respectively, 0.0, -0.1 and -0.2 eV going from top row to bottom row) measured at T = 80 K vs photon energy. In each image the intensity is averaged across 50 meV width.

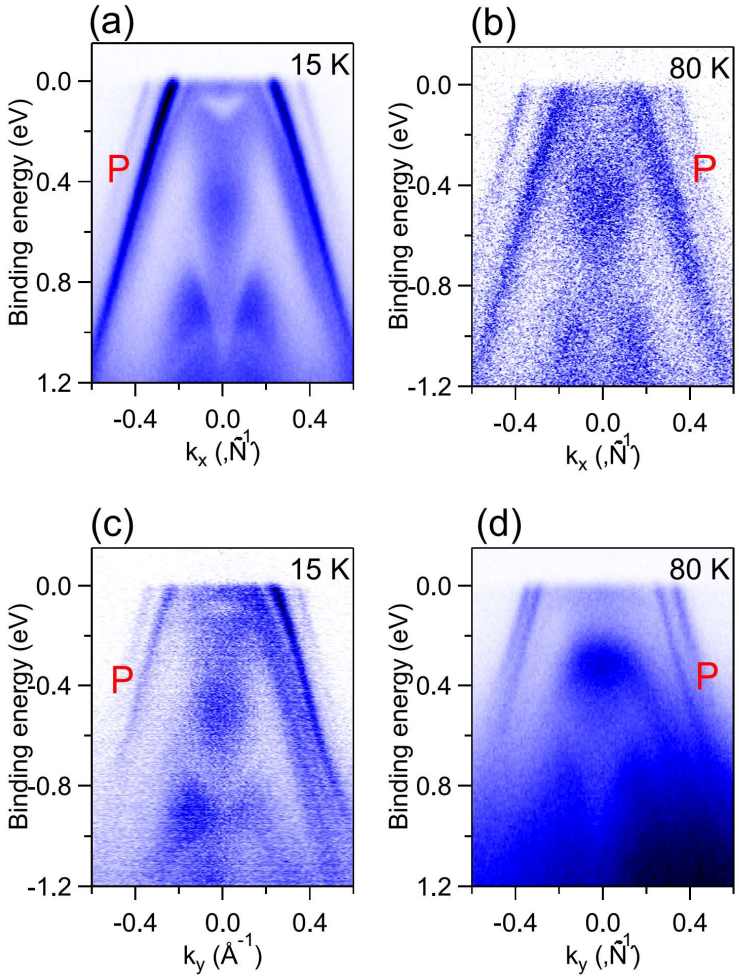

Fig. S6. Temperature dependent ARPES. ARPES maps measured below and above $T_{Néel}$ along $\bar{K}' - \bar{\Gamma} - \bar{K}$ (a,b) and $\bar{M}' - \bar{\Gamma} - \bar{M}$ (c,d) directions with $h\nu$ = 27 eV.

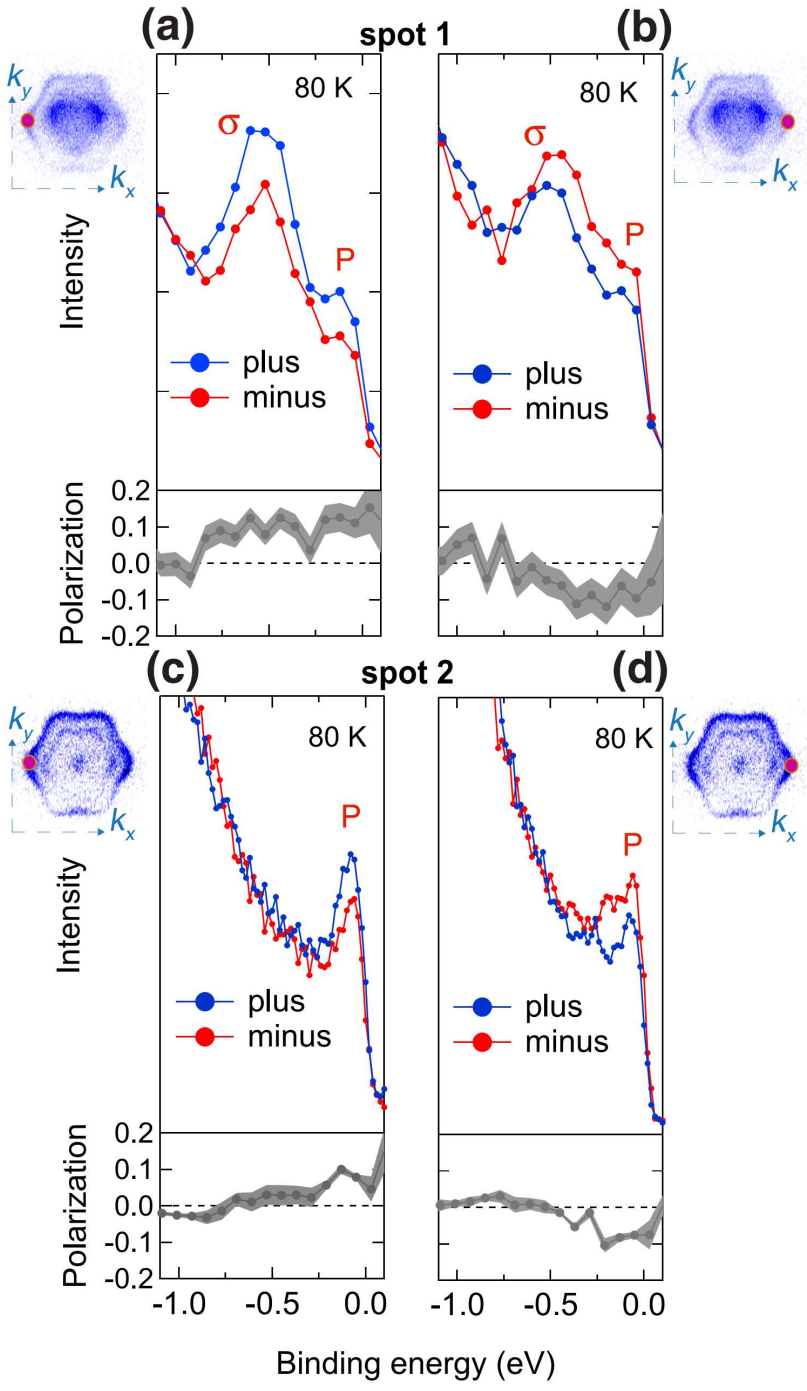

Fig. S7. Spin inversion above $T_{Néel}$. Spin resolved EDC cuts at fixed momentum (indicated for each panel as magenta dot in the insets, displaying Fermi surface color map) measured at 80 K with $h\nu$ = 27 eV along *y* direction in laboratory frame (as defined in the main text). The measurement is performed in two different spots at opposite momentum values (respectively, panel (a) and (b) for spot 1, and panel (c) and (d) for spot 2).

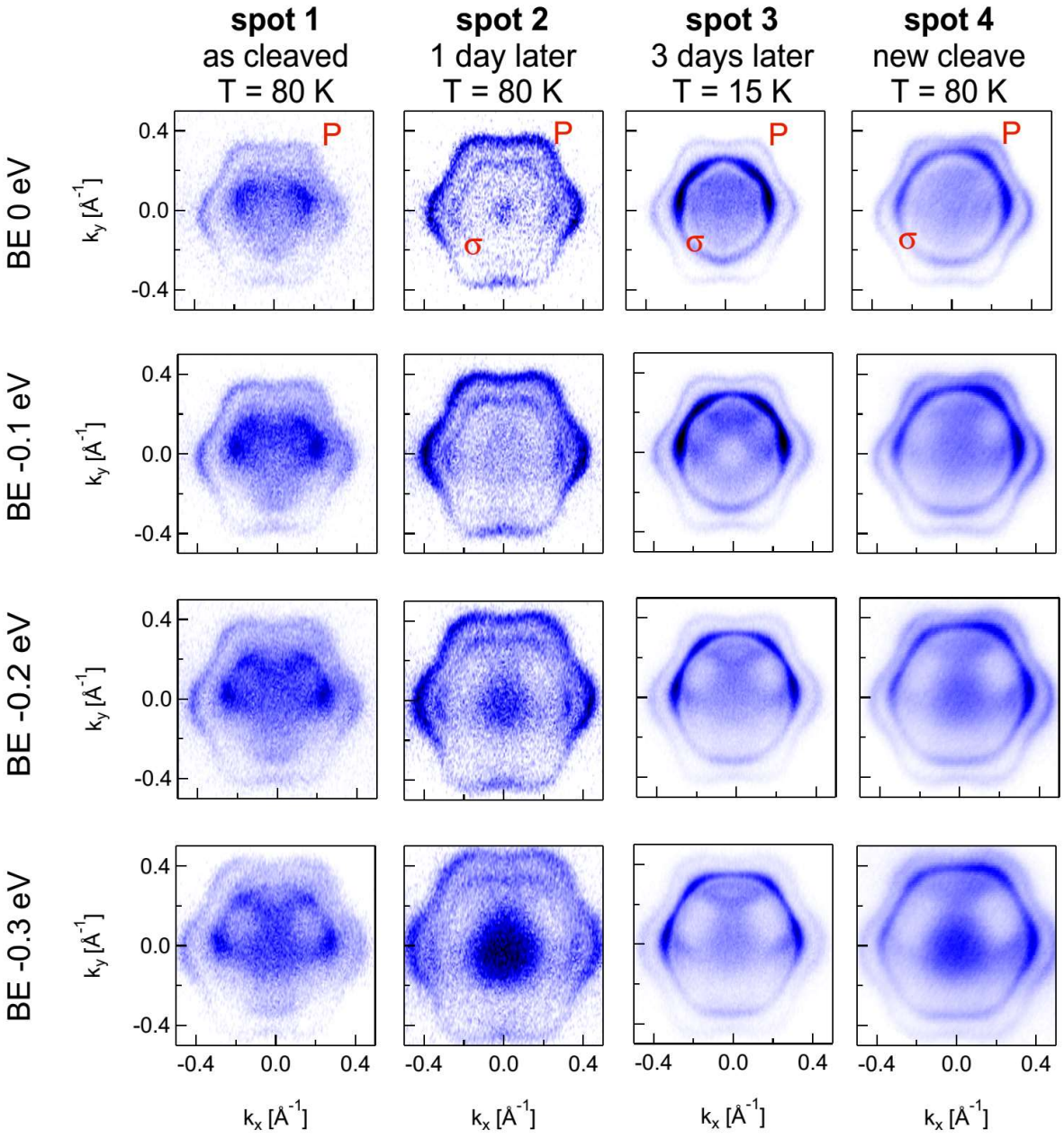

Fig. S8. ARPES in different spots. Isoenergetic ARPES cuts at fixed BE (respectively 0.0 eV, -0.1 eV, -0.2 eV and -0.3 eV) measured in different spots of the sample, with photon energy of 27 eV (spot 3 at T = 15 K, all other spots at T = 80 K).

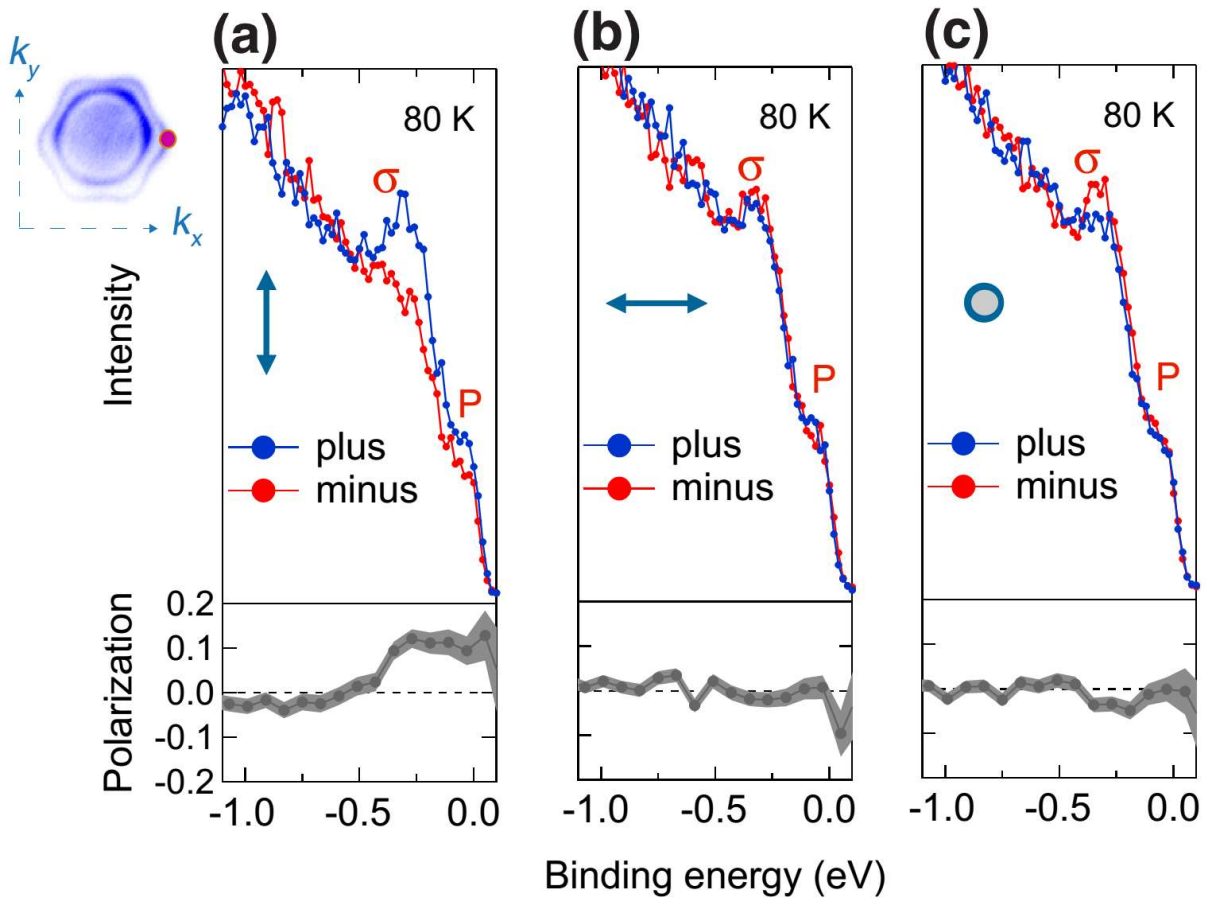

Fig. S9. Spin measurement along all directions. Spin resolved EDC cuts at fixed momentum (indicated as magenta dot in the Fermi surface color map) measured at 80 K with $\boldsymbol{h\nu}$ = 27 eV in all three spatial directions: *y* component in panel (a), *x* in panel (b) and *z* in panel (c).

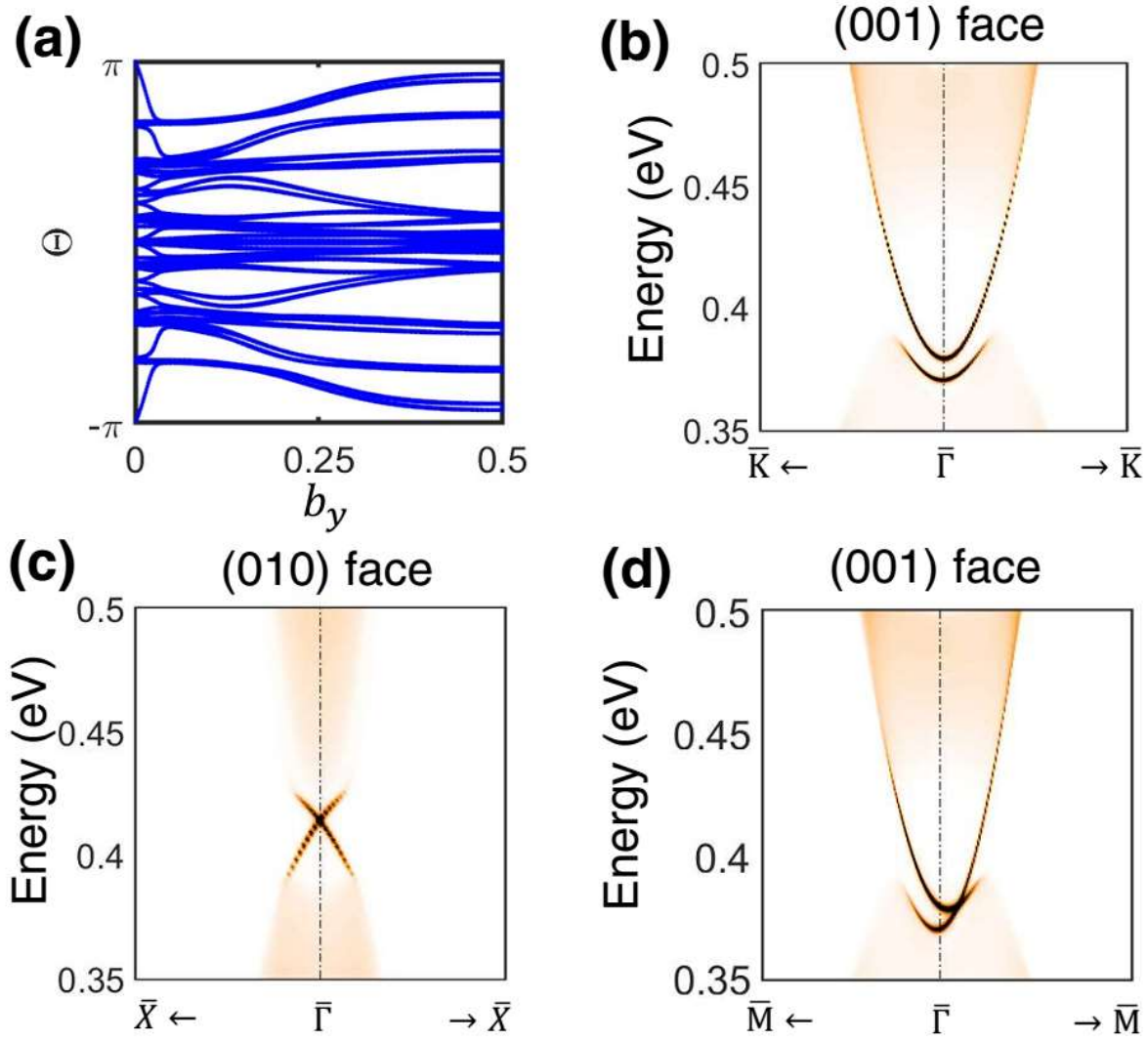

Fig. S10. Topology of the surface state. (a) Wannier charge center (WCC) evolution along k_y in the k_z = 0 plane. The trajectory of WCC is an open curve traversing the whole BZ, indicating the nontrivial Z_2 invariant, Z_2 = 1 (6). (b,d) Calculated surface spectral weight at different crystallographic planes in AFM phase: on (001) crystal face along $\bar{\Gamma} - \bar{K}$ direction (b), (010) face along $\bar{\Gamma} - \bar{X}$ direction (c), and (001) along $\bar{\Gamma} - \bar{M}$ direction (d).

Refined Formula	$EuSn_2P_2$
F.W. (g/mol)	451.28
Space group; Z	*R* -3*m*; 3
a(Å)	4.0927 (1)
c(Å)	26.119 (1)
V ($Å^3$)	378.89 (3)
Extinction Coefficient	0.0015 (3)
θ range (º)	2.339-31.545
No. reflections; R_{int}	2618; 0.0341
No. independent reflections	198
No. parameters	10
R_1: ωR_2 (I>2 (I))	0.0156; 0.0324
Goodness of fit	1.367
Diffraction peak and hole (e^-/ $Å^3$)	0.933; -1.384

Table S1. Single crystal structure refinement for $EuSn_2P_2$ at 302 (2) K.

Atom	Wyck.	Occ.	*x*	*y*	*z*	U_{eq}
Eu1	3*a*	1	0	0	0	0.0109 (2)
Sn2	6*c*	1	0	0	0.2110 (1)	0.0113 (2)
P3	6*c*	1	0	0	0.4054 (1)	0.0102 (3)

Table S2. Atomic coordinates and equivalent isotropic displacement parameters for $EuSn_2P_2$ at 302 K. (U_{eq} is defined as one-third of the trace of the orthogonalized U_{ij} tensor ($Å^2$))

Atom	U11	U22	U33	U23	U13	U12
Eu1	0.0092 (2)	0.0092 (2)	0.0142 (2)	0	0	0.0046 (1)
Sn2	0.0108 (2)	0.0108 (2)	0.0123 (2)	0	0	0.0054 (1)
P3	0.0094 (4)	0.0094 (4)	0.0119 (6)	0	0	0.0047 (2)

Table S3. Anisotropic thermal displacements from $EuSn_2P_2$.

SI References

1. X. Gui, *et al.*, A New Magnetic Topological Quantum Material Candidate by Design. *ACS Cent. Sci.* **5**, 900–910 (2019).
2. C. L. Kane, E. J. Mele, Z 2 Topological Order and the Quantum Spin Hall Effect (2005) https:/doi.org/10.1103/PhysRevLett.95.146802.
3. L. Fu, C. L. Kane, E. J. Mele, Topological Insulators in Three Dimensions (2007) https:/doi.org/10.1103/PhysRevLett.98.106803.
4. F. Schindler, *et al.*, Higher-order topological insulators. *Sci. Adv.* **4**, eaat0346 (2018).
5. C. Yue, *et al.*, Symmetry-enforced chiral hinge states and surface quantum anomalous Hall effect in the magnetic axion insulator Bi2–xSmxSe3. *Nat. Phys.* **15**, 577–581 (2019).
6. R. Yu, X. L. Qi, A. Bernevig, Z. Fang, X. Dai, Equivalent expression of Z2 topological invariant for band insulators using the non-Abelian Berry connection. *Phys. Rev. B - Condens. Matter Mater. Phys.* **84**, 075119 (2011).